A method for estimating global subgrid-scale gravity-wave temperature perturbations in chemistry-climate models

M. Weimer[1], C. Wilka[1,2], D. E. Kinnison[3], R. R. Garcia[3], J. Bacmeister[4], M. J. Alexander[5], A. Dörnbrack[6], S. Solomon[1]

[1]Department of Earth, Atmospheric and Planetary Sciences, Massachusetts Institute of Technology, Cambridge, MA, USA
[2]Department of Earth System Science, Stanford University, Stanford, CA, USA
[3]Atmospheric Chemistry Observations & Modeling Laboratory, National Center for Atmospheric Research, Boulder, CO, USA
[4]Climate and Global Dynamics Laboratory, National Center for Atmospheric Research, Boulder, CO, USA
[5]NorthWest Research Associates/Colorado Research Associates, Boulder, Colorado, USA
[6]Institut für Physik der Atmosphäre, Deutsches Zentrum für Luft und Raumfahrt, Oberpfaffenhofen, Germany

Key Points:

- We present a method for estimating subgrid scale gravity wave temperature perturbations on a global scale
- The distributions of the perturbations are compared with COSMIC and ERA5 to estimate scaling factors
- These temperature perturbations impact stratospheric aerosols and chemistry particularly near the tropical tropopause and polar regions

Corresponding author: Michael Weimer, `mweimer@mit.edu`

Abstract

Many chemical processes depend non-linearly on temperature. Gravity-wave-induced temperature perturbations have been previously shown to affect atmospheric chemistry, but accounting for this process in chemistry-climate models has been a challenge because many gravity waves have scales smaller than the typical model resolution. Here, we present a method to account for subgrid-scale orographic gravity-wave-induced temperature perturbations on the global scale for the Whole Atmosphere Community Climate Model (WACCM). The method consists of deriving the temperature perturbation amplitude $\hat{T}$ consistent with the model's subgrid-scale gravity wave parametrization, and imposing $\hat{T}$ as a sinusiodal temperature perturbation in the model's chemistry solver. Because of limitations in the gravity wave parameterization, scaling factors may be necessary to maintain a realistic wave amplitude. We explore scaling factors between 0.6 and 1 based on comparisons to altitude-dependent $\hat{T}$ distributions in two observational datasets. We probe the impact on the chemistry from the grid-point to global scales, and show that the parametrization is able to represent mountain wave events as reported by previous literature. The gravity waves for example lead to increased surface area densities of stratospheric aerosols. This in turn increases chlorine activation, with impacts on the associated chemical composition. We obtain large local changes in some chemical species (e.g., active chlorine, NO_x, N_2O_5) which are likely to be important for comparisons to airborne or satellite observations, but find that the changes to ozone loss are more modest. This approach enables the chemistry-climate modeling community to account for subgrid-scale gravity wave temperature perturbations in a consistent way.

Plain Language Summary

Sub-grid scale gravity waves have long been considered in the momentum budgets of global chemistry-climate models using parameterizations, but their associated impacts on temperature perturbations have not been included in chemical schemes in a self-consistent way. Here we present an approach to modeling these chemical impacts in the Whole Atmosphere Community Climate Model (WACCM). We obtain large local changes in some chemical species (e.g., active chlorine, NO_x, N_2O_5) but smaller impacts on ozone. The approach can be expected to advance the ability of the chemistry-climate modelling community to examine gravity wave effects on a wide range of chemical problems.

1 Introduction

A number of chemical processes are strongly exponentially dependent on the temperature (Burkholder et al., 2015), and the formation of stratospheric aerosols is linked to temperature thresholds (Hanson & Mauersberger, 1988; Marti & Mauersberger, 1993; Carslaw et al., 1994; Eckermann et al., 2006; Solomon et al., 2015). As a consequence, small-scale variations of the temperature, that arise for example from wave-like perturbations, can change the concentrations of atmospheric trace gases despite an unchanged averaged temperature across the wave motion since

$$k(\overline{T}) \neq \overline{k(T)} \tag{1}$$

where k is a heterogeneous or gas-phase reaction rate constant and T is temperature (e.g., Murphy & Ravishankara, 1994). Even small-scale temperature perturbations can be important for highly nonlinear chemistry and should in principle be accounted for in chemistry-climate models.

Examples of waves leading to such temperature perturbations include Kelvin, Rossby and gravity waves (Madden, 1979; Fritts & Alexander, 2003; Das & Pan, 2013). While the planetary scale Kelvin and Rossby waves can be resolved by current chemistry-climate models (Eyring et al., 2016; Knippertz et al., 2022), a significant fraction of the gravity wave spectrum occurs on the subgrid scales of current models.

Gravity waves are generated by various sources including orography and convection, and can propagate horizontally and vertically in a stably stratified atmosphere. These waves have been shown to affect the atmosphere's dynamical structure, especially of the stratosphere and mesosphere (see Fritts & Alexander, 2003, for an overview). Here, we focus on orographic gravity waves (OGWs). Many hot spots of OGW generation have been identified in the literature: the Scandinavian Mountains, Iceland, Svalbard, Greenland, Ural Mountains, Rocky Mountains and the Himalayas in the Northern Hemisphere and the Andes, the Antarctic Peninsula, the Transantarctic Mountains, New Zealand and various small islands in the Southern Hemisphere (S. P. Alexander et al., 2009; Krisch et al., 2017; Dörnbrack et al., 2017; Lilly et al., 1982; Vosper et al., 2020; Hoffmann et al., 2013; Kaifler et al., 2020; Taylor et al., 2019; Jackson et al., 2018; Rapp et al., 2021).

Properties of gravity waves can be measured by satellite instruments on a global scale (Anthes et al., 2008; Hoffmann & Alexander, 2009) and locally by radiosondes, aircraft campaigns, or lidar instruments (e.g., Leena et al., 2012; Rapp et al., 2021; Kaifler et al., 2020). Radio occultation satellite measurements, such as those by the Constellation Observing System for Meteorology Ionosphere and Climate/Formosa Satellite 3 (COSMIC) mission (Anthes et al., 2008), have been shown to provide high-accuracy measurements of gravity wave temperature perturbations with daily global coverage (e.g., Wang & Alexander, 2010). In addition, recent reanalysis products like the ECMWF Reanalysis version 5 (ERA5) have been shown to resolve parts of the gravity wave spectrum (Hoffmann et al., 2019; Gupta et al., 2021; Dörnbrack et al., 2020; Dörnbrack, 2021; Dörnbrack et al., 2022; Rapp et al., 2021). Stratospheric gravity wave-driven temperature perturbations as large as 40 K have been measured (Kaifler et al., 2020). The subgrid-scale effects of such waves on the momentum budget are a necessary component of global climate models (e.g., Bacmeister et al., 1994; Fritts & Alexander, 2003; Garcia et al., 2017; Giorgetta et al., 2018; Kruse et al., 2022), providing the framework needed to examine their associated impacts on the global chemistry.

The first studies investigating this process accounted for the impact of gravity-wave-induced temperature perturbations on polar stratospheric clouds (PSCs) via Lagrangian or mesoscale modeling (Carslaw et al., 1998; Fueglistaler et al., 2003; Mann et al., 2005; Eckermann et al., 2006; Noel & Pitts, 2012), but they had to apply it as a post-processing step rather than an interactive calculation on the global scale. Weimer et al. (2021) used a local grid refinement approach with two-way interaction to simulate the global impact of a mountain wave event around the Antarctic Peninsula. Such approaches can only be applied for specific known gravity wave events or specific hot spots due to their high computational costs. Kärcher et al. (2019) examined the potential role of gravity waves in cirrus cloud formation, but associated chemical impacts were not considered. Only one other study has attempted to include the temperature effect of gravity waves in a global chemistry model: Orr et al. (2020) parametrized orographic gravity waves to the PSC scheme in the U.K. Unified Model and showed impacts on chlorine activation and the related ozone chemistry, but only considered the cold phase of the wave.

Here we present a method to account for both the cold and warm phases of subgrid scale gravity waves on the global scale in a widely used community model. The method consists of derivation of temperature perturbation amplitudes from the gravity wave parametrization and its application to the chemistry. We briefly describe the model and the method in Sect. 2, and then evaluate the modelled temperature amplitudes $\hat{T}$ with COSMIC measurements and ERA5 reanalysis data in Sect. 3. We show examples of the calculated impacts of the gravity wave temperature effects on chemical concentrations in the stratosphere in Sect. 4, and finally discuss implications of and future directions for this study in Sect. 5.

2 WACCM

The testbed for this study is the Specified Dynamics (SD) version of the Whole Atmosphere component (WACCM6) of the Community Earth System Model (CESM2.1) (Gettelman et al., 2019; Danabasoglu et al., 2020). Specified dynamics are used in order to readily compare single runs with and without the effects of the gravity waves, which could be difficult to separate from other sources of dynamical variability in free-running simulations. Here, the model is relaxed to the Modern-Era Retrospective Analysis for Research and Applications version 2 (MERRA2, Gelaro et al., 2017) using the FWSD component set (see Gettelman et al., 2019, for the definition). The relaxation is applied only between the surface and 1 hPa, which is why we restrict our analysis to this pressure range in this study. Horizontal discretization is done on a 1.25°x0.9° longitude-latitude grid on 88 vertical levels up to about 140 km. The lower stratospheric vertical grid spacing is on the order of 1 km (e.g., Garcia et al., 2017). The physics time step is set to 30 minutes. This is also the standard time step used in the chemistry modules but here we examine the need for shorter time steps to capture gravity wave impacts on chemistry. See below for discussion of chemistry time stepping in this study.

Detailed chemistry for the troposphere, stratosphere, mesosphere and lower thermosphere is calculated in WACCM (Kinnison et al., 2007; Emmons et al., 2020), including heterogeneous processes on tropospheric and stratospheric particles and clouds (e.g., Wegner et al., 2013; Solomon et al., 2015).

The OGW parametrization of WACCM consists of a source specification and a wave propagation model. The propagation model assumes two dimensional steady-state hydrostatic waves as was done by McFarlane (1987) for OGW and has been extended to other sources of gravity waves in WACCM (Richter et al., 2010). The parameterized OGW are assumed to conserve wave momentum flux $\rho\overline{u'w'}$ until wave breaking occurs, where ρ is the air density and u' and w' are the horizontal and vertical wind perturbation of the wave, respectively. Breaking occurs when the wave $u' \sim \overline{U}$, either as a consequence of exponential density decrease with altitude or as a consequence of the shape of the mean wind profile $\overline{U}$.

We use the momentum flux calculated by the gravity wave parametrization to derive a temperature perturbation amplitude $\hat{T}$ using Eq. 7 by Ern et al. (2004):

$$\left|\hat{T}\right| = \hat{h}\frac{\partial\overline{\theta}}{\partial z}\frac{\overline{T}}{\overline{\theta}} \tag{2}$$

with

$$\hat{h} = \sqrt{\frac{\tau}{\overline{\rho}\,N\,\left|\overline{U}-c\right|\,k_{\mathrm{h}}}} \tag{3}$$

In these equations, $\overline{\theta}$ and $\overline{T}$ stand for the grid-scale potential temperature and air temperature, respectively, and z is the geometric altitude. The vertical displacement amplitude $\hat{h}$ is derived from the gravity wave momentum flux τ, the grid-scale air density $\overline{\rho}$, the Brunt-Väisälä frequency N, the difference between grid-scale horizontal wind speed perpendicular to the mountain range $\overline{U}$ and the phase speed c, and the horizontal wavenumber k_{h}. For steady-state OGWs phase speeds are zero.

In the current WACCM OGW scheme, parameters describing the unresolved orography that forces parameterized OGW are determined using a "ridge-finding" algorithm (cf. Kruse et al., 2022, Appendix B). The algorithm returns estimates of orientation a_r, obstacle height h_r, and width w_r for unresolved topographic features. The orientation a_r is used to determine the wave-relevant mean wind profile $\overline{U}$ from the model horizontal wind. We identify the obstacle height with the wave vertical displacement at the surface, i.e., $d(z = 0) = h_r$. The relationship between the estimated obstacle width w_r

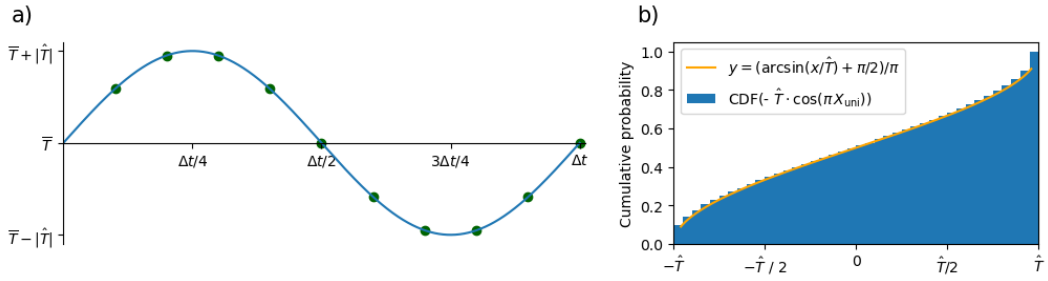

Figure 1. Illustration of (a) the temperature evolution in the sub-stepping approach using temporal sub-stepping (green dots) and (b) the stochastic approach using a sine-wave-distributed random T'.

and the monochromatic horizontal wavenumber is not straightforward. The dominant scale of waves launched by a real-world (non-sinusoidal) obstacle will depend on the shape of the obstacle as well as on features of the low-level flow such as blocking or flow diversion (e.g., Smith & Kruse, 2017, 2018). In this study we assume the simple relation $k_{\mathrm{h}} = 1/w_r$.

Consistent with previous studies we will refer to $\hat{T}$ as the (non-negative) temperature amplitude and T' as the temperature perturbation of the gravity wave (e.g., Schmidt et al., 2016):

$$T'(\vec{r},t) = \hat{T}(\vec{r},t) \cdot \sin\left(\vec{k}\cdot\vec{r} - \omega t\right) \tag{4}$$

where $\vec{k}$ and ω are 3-D spatial and temporal wavenumbers, respectively, and $\vec{r}$ is the 3-D location vector.

We simulate the influence of the wave-driven temperature excursions in two ways, by temporal sub-stepping and stochastically. In the sub-stepping method, we use the absolute value of $\hat{T}$ from Eq. 2 at each model grid point as the amplitude of a sine wave and change the temperature within the chemistry by sampling the wave at ten intermediate timesteps as depicted in Fig. 1a, with a corresponding reduction of the chemistry time step to 3 min compared to the standard timestep of 30 min in this model. This sub-stepping includes the calculations of polar stratospheric clouds (PSCs), tropospheric aerosols, reaction rate constants, photolysis rates, washout rates, chemistry solvers and settling of nitric acid trihydrate (NAT) particles. This method has the advantage of ensuring consistent evolution of multiple chemical species that may be interdependent in the same manner that an air parcel moving through the grid box would experience the effect of the wave. The sub-stepping approach assumes that all phases of the gravity wave temperature perturbations are sampled within one 30-minute model time step. Assuming parcels are exposed to one wave cycle every 30 minutes is equivalent to assuming the wave intrinsic period (ν) is 30 min. Using the OGW dispersion relation $\lambda/\nu = \overline{U}$, this would be strictly accurate for mesoscale gravity waves of order $\lambda = 100$ km only in conditions of strong winds order 50 m s^{-1}, but is reasonable for polar vortex conditions.

However, sub-stepping through the chemistry on 3 minute timesteps while the dynamics and dynamical-chemical coupling is calculated using the physics timestep of 30 minutes increases the overall model computation time by a factor of two and appears to lead to some artifacts in the chemical tracers at around 1 hPa, see Sect. 4. We also consider an alternative stochastic approach using sine-wave-distributed random T' without any sub-stepping. In this approach, T' is computed from a uniformly distributed ran-

Table 1. Simulations in this study.

Name	Remark
REF	Reference simulation without $\hat{T}$ parametrization
Sub-stepping (scaled)	Simulation with $\hat{T}$ scaled as discussed in Sect. 3
Sub-stepping (non-scaled)	Simulation with non-scaled $\hat{T}$
Stochastic (scaled)	Simulation using sine-wave-distributed random $\hat{T}$, scaled as discussed in Sect. 3

dom variable X_{uni} between 0 and 1 by

$$T'_{\mathrm{stoch}}(\vec{r},t) = -\hat{T}(\vec{r},t) \cdot \cos\left(\pi\, X_{\mathrm{uni}}\right), \quad X_{\mathrm{uni}} \in [0,1) \tag{5}$$

which is shown in Fig. 1b.

OGW events usually last longer than one day with similar amplitude (e.g., S. P. Alexander et al., 2009; Noel & Pitts, 2012). This means that the wave of Fig. 1a is sampled at 48 stochastically chosen phases per day when using a physics time step of 30 minutes, so that the overall response of the chemistry to the temperature perturbation could be similar in long-term averages, although differences can be expected when looking at single time steps. Holding stochastically chosen T' for 30 minutes at a time is equivalent to assuming that the intrinsic period of the wave $\nu \gg 30\,\mathrm{min}$, 2-3 hours or more. This case would be more strictly true for the $\lambda = 100\,\mathrm{km}$ gravity wave in slower wind conditions $\sim 9 - 13\,\mathrm{m\,s^{-1}}$.

Another approach to decrease the overall computation time could be to apply the sub-stepping approach and sample the wave at fewer points than shown in Fig. 1a. Sensitivity simulations decreasing the number of sub-steps showed systematic differences compared to ten-fold sub-stepping in the chemistry response. A number of sub-steps larger than ten were found to lead to no large differences compared to ten-fold. Therefore, we restrict the analysis in this study to ten-fold sub-stepping, as shown in Fig. S1 in the supplement.

The steps to implement this approach in the model consist of (1) adding Eq. 2 to the model, (2) add the temperature perturbation to the grid-scale temperature using either Eq. 4 and surround the chemistry routines by a loop with subsequent reduction of the time step or Eq. 5 without sub-stepping and (3) apply the perturbed temperature to all selected routines in the chemistry code. In addition, the scaling, discussed in the next section, has to be accounted for.

We performed simulations with and without the $\hat{T}$ parametrization, see Table 1 and Sect. 3 below regarding scaling. We chose the period 2007 to 2008 for the simulations presented here because it has the best coverage of the COSMIC measurements we use for comparison, see Sect. 3 and Appendix A. Daily maximum and averages as well as monthly averages are provided as output to investigate the chemical impact of the new parametrization.

As an example, Figure 2 shows the global distribution of the the two-year maximum $\hat{T}$ at 15 hPa in WACCM. Since the method is applied to OGWs in this study, $\hat{T}$ is largest in the mountainous regions on the globe. The hot spots of orographic gravity waves show increased $\hat{T}$ values, e.g., over the Antarctic Peninsula, the Andes and New Zealand in the Southern Hemisphere as well as Scandinavia, Greenland, the Ural Mountains, the European Alps, Apennines, the Carpathians and the Rocky Mountains in the Northern Hemisphere. Lower-level wind speeds vary seasonally in the model, leading to

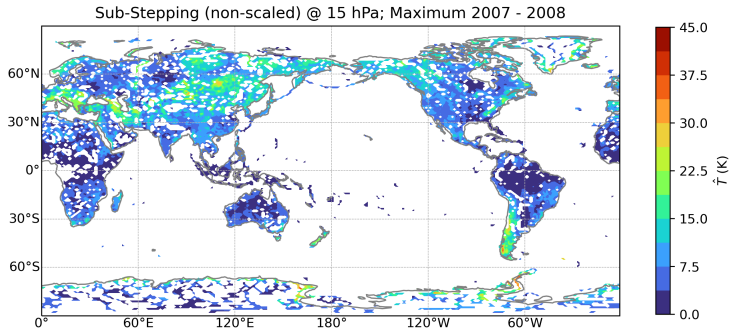

Figure 2. Two-year maximum $\hat{T}$ at 15 hPa as simulated by WACCM.

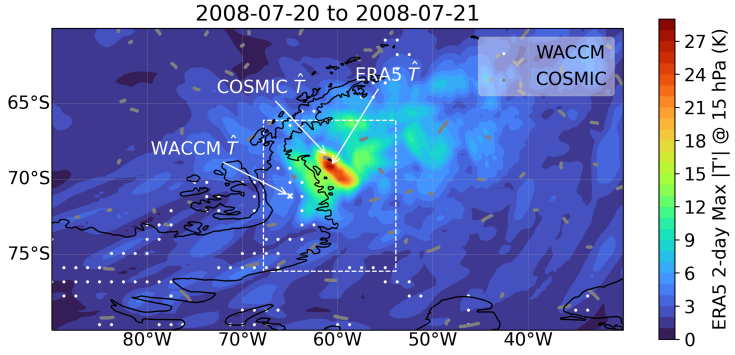

Figure 3. Illustration of the different coverage of each dataset: white points are WACCM grid points with $\hat{T} > 4$ K anywhere in the column where COSMIC and ERA5 are reliable, COSMIC profiles between 14 and 34 km are shown by the gray lines and ERA5 is color-coded. The example shown is for a two-day period, for details see text. The white dashed region is used for best estimates of $\hat{T}$ for all datasets.

associated seasonal gravity wave and temperature amplitudes (e.g., Hoffmann et al., 2013) which will be briefly discussed in Sect. 3.

There are numerous limitations of the OGW parametrization of WACCM that could affect calculated $\hat{T}$ (e.g. no lateral propagation, no dispersion, no wave-wave interaction, no damping other than that due to breaking). Because of these limitations and an expected overestimation of temperature amplitudes at higher altitudes, we seek to compare our estimated $\hat{T}$ values against other datasets, which is the subject of the next section.

3 Scaling of the new $\hat{T}$ parametrization by means of ERA5 and COSMIC

Since WACCM $\hat{T}$ is calculated globally, we focus on datasets that provide global coverage with high vertical resolution and discuss methods to compare WACCM $\hat{T}$ globally with these datasets. Satellite-based radio occultation measurements as well as recent reanalysis data have been shown to satisfy these requirements (Wang & Alexander, 2010; Dörnbrack, 2021). We therefore use COSMIC and ERA5. Details about COSMIC, ERA5, and the methods to extract the gravity wave temperature perturbations are described in Appendix A.

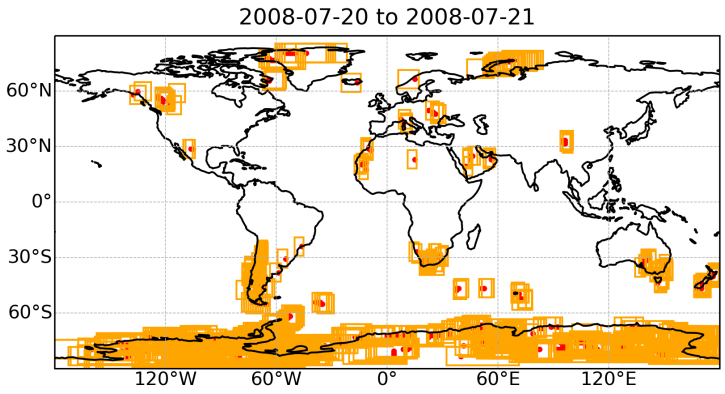

Figure 4. Illustration of the regions over the globe where significant OGW forcing occurs in WACCM (orange) and the corresponding grid points (red) during 20 to 21 July 2008.

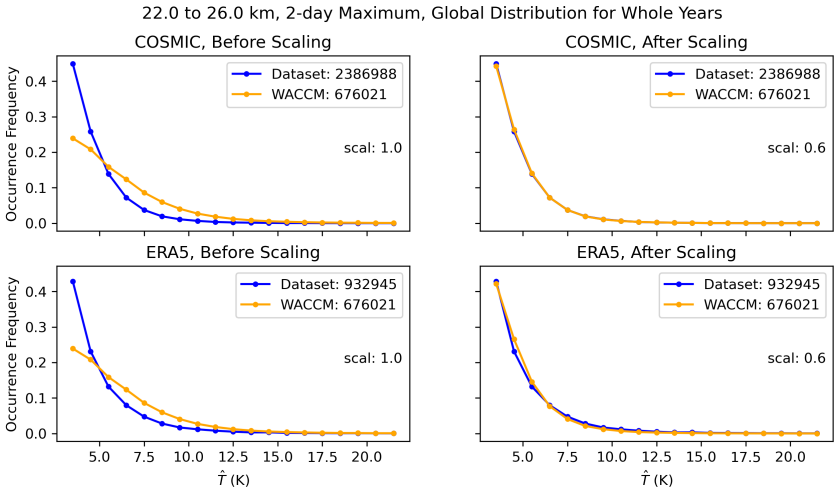

Figure 5. Probability density functions of $\hat{T}$ for WACCM (orange) and the respective dataset (blue) in the 4-km altitude bin 22 to 26 km and the scaling factors that minimize the differences between the probability density functions. By applying a scaling factor of 0.6 to $\hat{T}$, the number of grid points in WACCM with lower $\hat{T}$ decreases.

There are fundamental differences between measurements by COSMIC, the ERA5 reanalysis, and coverage of WACCM: As shown in Fig. 2, WACCM $\hat{T}$ is only significant over the mountains, i.e. over land. Lateral propagation of gravity waves from one grid point to another cannot be simulated in WACCM because the parameterization operates in column physics. In reality, OGWs propagate not only vertically but also horizontally so that wave signals in COSMIC and ERA5 will often occur in the lee of mountains instead of only over the mountain. In addition, COSMIC provides measurements at irregularly distributed locations whereas ERA5 outputs hourly global coverage. This is illustrated in Fig. 3 where COSMIC profiles during a two-day period around the Antarctic Peninsula are denoted by gray points, the WACCM grid points with a $\hat{T}$ are depicted by white dots, and ERA5 is color-coded. Finally, COSMIC and ERA5 data are instantaneous temperature perturbations $T'(\vec{r}_0, t_0)$ whereas we decided to output daily statistics of the temperature amplitude $\hat{T}$ in WACCM, cf. Eq. 4. As indicated by Fig. 1 and Eq. 4, the wave amplitude is the maximum temperature perturbation:

$$\hat{T} = \max |T'| \tag{6}$$

Therefore, we compare WACCM $\hat{T}$ with COSMIC and ERA5 on a global scale as described below.

The goal is to find the values in COSMIC and ERA5 that most likely correspond to the temperature amplitudes $\hat{T}$ in WACCM. The maximum T' for COSMIC and ERA5 is searched for in a region around the WACCM columns where non-zero $\hat{T}$ values are calculated. Since horizontal coverage is crucial for this procedure to ensure a COSMIC profile to be at the location of the maximum, only the WACCM columns are used where at least five COSMIC profiles are included in the regions, similar to the analysis by S. P. Alexander et al. (2009). Further, the maximum of n days is calculated where we will show a sensitivity study with $2 < n < 7$ which corresponds to the usual length of gravity wave events (e.g., S. P. Alexander et al., 2009; Noel & Pitts, 2012). An example for $n = 2$ is shown in Figures 3, 4, and 5.

Since $\hat{T}$ is the amplitude of a sine wave, this should capture the impact of observed gravity waves in the data, cf. Fig 1. In Sect. 4, it will be shown that WACCM $\hat{T} > 4\,\mathrm{K}$ can be connected to specific gravity wave events reported by the literature, see Fig. 8. Therefore, we use the WACCM columns with $\hat{T} > 4\,\mathrm{K}$ anywhere in the altitude range between 14 and 34 km where both COSMIC and ERA5 are reliable. In order to account for the horizontal propagation of the gravity waves, the zonal extension of the region around the WACCM columns is set to half of the largest scale gravity wave resolved in the ERA5 perturbations (i.e. 500 km, see Appendix A) shifted by 400 km towards the lee of the mountain. In the meridional direction, the region extends to $\pm 5°$ around the WACCM grid point. An example of one region is illustrated by the white dashed lines in Fig. 3. This is done all over the globe, which can be seen in Fig. 4 for the same two-day period as shown in Fig. 3.

Altitude-dependent probability density functions of $\hat{T}$ in 4-km height bins are calculated for all the datasets, see the example in Fig. 5 for the height bin of 22 to 26 km. As might be expected due to the limitations of the parametrization, WACCM overestimates the large $\hat{T}$ values and underestimates low $\hat{T}$ values compared to both COSMIC and ERA5 (left column of Fig. 5). This is shown by a larger probability density of WACCM $\hat{T}$ for $\hat{T} > 5\,\mathrm{K}$. The WACCM $\hat{T}$ values are scaled by factors between 0.1 and 10 and the WACCM distribution with a scaling factor minimizing the distance between the global probability density functions is shown in the right column of Fig. 5. By applying a scaling factor of 0.6 to $\hat{T}$ in the example altitude bin of Fig. 5, the number of grid points in WACCM with smaller $\hat{T}$ increases accordingly.

As mentioned above, these scaling factors are calculated for each 4-km altitude bin and for varying the number of days to collect the maximum between 2 and 7. The resulting distributions of scaling factors for each altitude bin are shown in Fig. 6, together

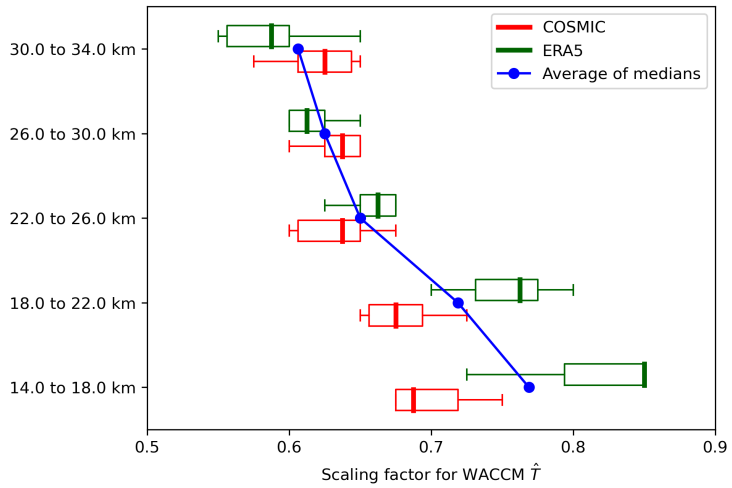

Figure 6. Altitude-dependent distributions of scaling factors using the method illustrated n Figures 3, 4 and 5 by varying the periods from 2 to 7 days to get max $\hat{T}$ for all datasets. The "scaled" experiments use this scaling profile for WACCM $\hat{T}$ with no scaling (scaling factor 1) at lower altitudes and a constant scaling factor above 34 km. The "non-scaled" experiment uses a scaling factor of 1 at all altitudes.

with the average of the medians of COSMIC and ERA5. The stratospheric scaling factors vary between 0.6 and 0.8 and increase towards 1 at lower altitudes. In the real world, waves are not monochromatic, so wavepackets can disperse (and thus reduce local amplitude) and they can also propagate laterally as already shown, whereas in WACCM the waves are confined to a column in which they grow as $\exp(z/2H)$ until they break. These limitations will become more and more relevant with increasing altitude, thus leading to the need to scale down the WACCM values more at higher altitude in order to bring the model into agreement with COSMIC. Both ERA5 and COSMIC will underestimate amplitudes of short λ gravity waves. COSMIC is generally only sensitive to $\lambda >$ 200 km except in conditions of fortuitous alignment of the satellite line-of-sight with the wave's lines of constant phase (M. J. Alexander, 2015; Schmidt et al., 2016). ERA5 will also damp OGWs with wavelengths smaller than about 160 km due to limited resolution, and previous studies show effects of the ECMWF model system resolution on OGW temperature amplitudes (Hoffmann et al., 2017; Kruse et al., 2022; Polichtchouk et al., 2022). Hence, temperature amplitudes are probably overestimated by WACCM but underestimated by the datasets which is why we will show results of simulations using the scaling profile of Fig. 6 and unscaled results, see also Table 1.

Due to the seasonal cycle of surface wind and thus gravity wave activity (Hoffmann et al., 2013), $\hat{T}$ also shows a seasonal cycle with largest values during local winter. Results of the monthly and zonal maximum $\hat{T}$ for the two WACCM simulations and ERA5 are shown in Fig. 7 for January and July 2008, i.e., one month in the respective winter seasons in each hemisphere.

The gap in WACCM $\hat{T}$ at around 60 °S can be explained by the fact that there are no mountains at this latitude generating gravity waves. Note that unlike the OGW parameterization in WACCM, OGWs can propagate horizontally, so they can propagate into the Drake Passage, which is why there is no corresponding gap in ERA5.

The $\hat{T}$ values increase with altitude. They reach values as high as 70 K in the non-scaled simulation, which has not been reported in measurements to date. Kaifler et al.

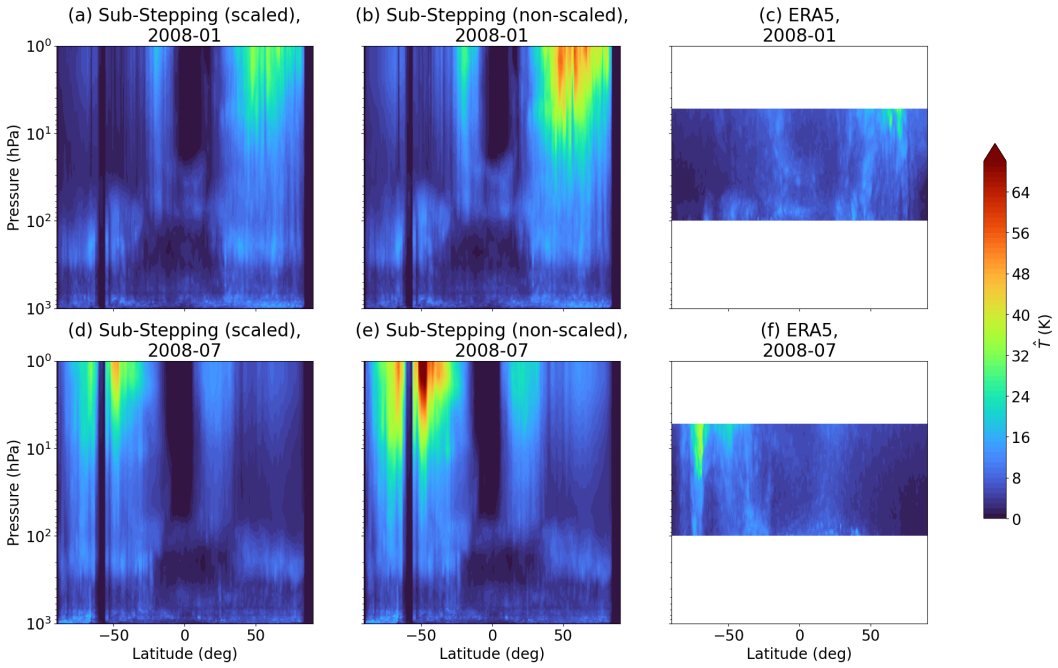

Figure 7. Zonal monthly maximum $\hat{T}$ in January (first row) and July 2008 (second row) for the (a,d) "Sub-stepping (scaled)" and (b,e) "Sub-stepping (non-scaled)" WACCM simulations and (c,f) ERA5. $\hat{T}$ in "Stochastic (scaled)" is the same as in "Sub-stepping (scaled)". For $p < 1$ hPa, the nudging of WACCM towards MERRA2 decreases with no nudging for $p < 0.3$ hPa, which is why the analysis in this study is restricted to lower altitudes, see also Sect. 2.

(2020) found upper stratospheric $\hat{T}$ values up to about 40 K above the Andes during an event in 2018. The scaling applied to $\hat{T}$ reduces these large values to the range observed by Kaifler et al. (2020). Figure 7 illustrates that the $\hat{T}$ values are comparable to ERA5 in pressure range between 5 and 20 hPa when the scaling profile is applied there. Thus, the scaled $\hat{T}$ values in WACCM are broadly consistent with observations in the stratosphere, and we will investigate illustrative impacts of both the scaled and unscaled $\hat{T}$ in this new parametrization on the stratospheric chemistry in the next section.

4 Impacts on the stratospheric chemistry

This section discusses the impact when applying the new $\hat{T}$ parametrization to the chemistry in WACCM. We focus the analysis of the influence in the stratosphere. As a first example, Figure 8 shows timeseries of the daily mean values of various variables at 15 hPa over two hot spots of orographic gravity waves: Svalbard (left column) in the Northern Hemisphere and the Antarctic Peninsula (right column) in the Southern Hemisphere (e.g., Dörnbrack et al., 2017; Noel & Pitts, 2012). Orange, blue and red and black lines in all panels correspond to the "Sub-stepping (non-scaled)", "Sub-stepping (scaled)", "Stochastic (scaled)" and "REF" simulations, respectively.

The two rows at the bottom of Fig. 8 show WACCM $\hat{T}$ and the absolute temperature with $\pm\hat{T}$ as colored shading and lines, respectively. Time intervals with substantial $\hat{T}$ values are simulated at both hot spots. In the case of the Antarctic Peninsula, the gray shaded time periods also indicate when gravity wave events were obtained in the mesoscale simulation by Noel and Pitts (2012) between June and August 2008. The good general agreement for the time periods with $\hat{T} > 4$ K (black dashed lines in the panel)

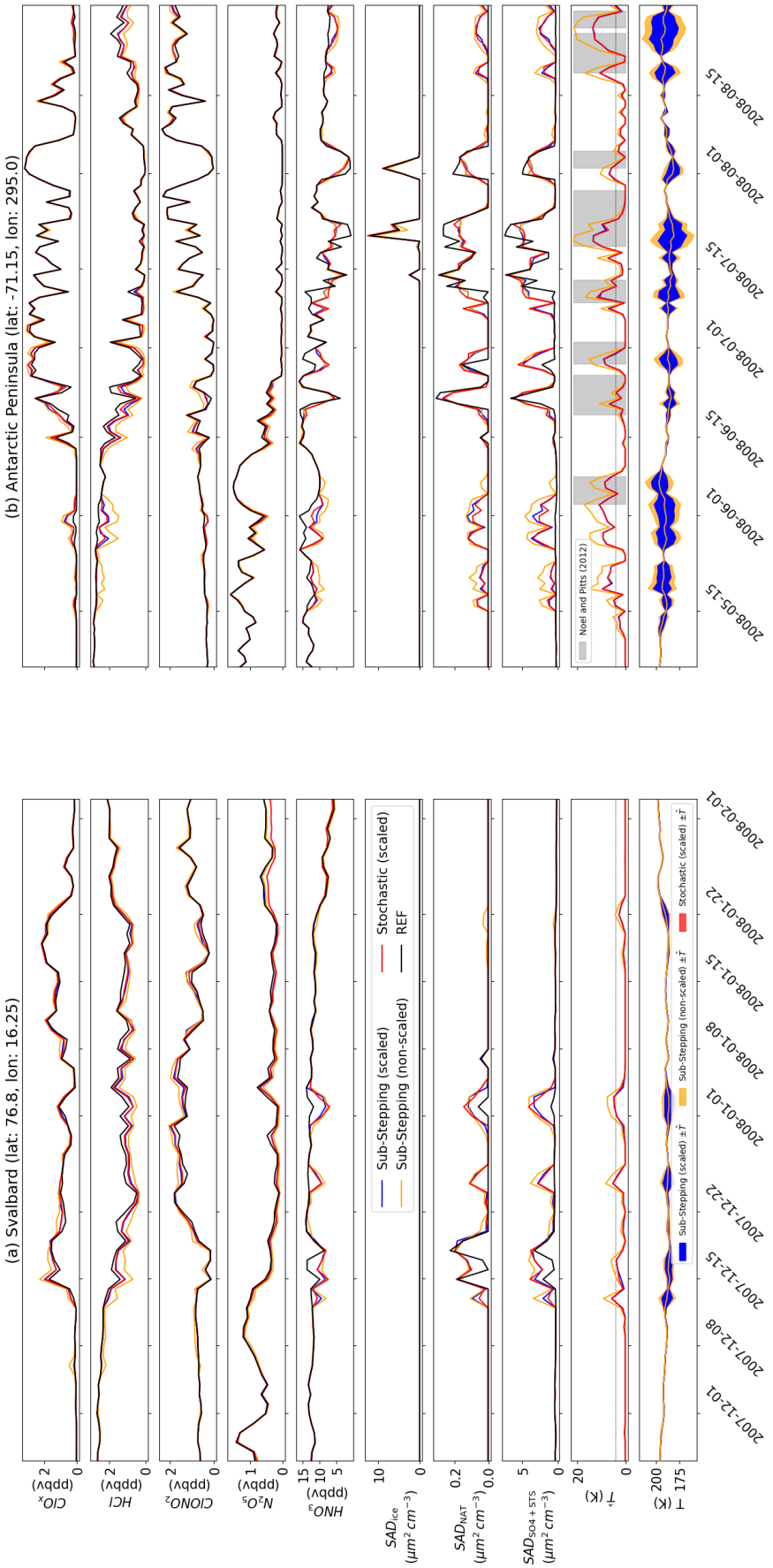

Figure 8. Timeseries of daily mean concentrations of different trace gases and aerosols at single WACCM grid points over (a) Svalbard and (b) the Antarctic Peninsula at 15 hPa. The lines correspond to the simulations of Table 1. The gray shaded regions in the timeseries over the Antarctic Peninsula are gravity wave events as reported by Noel and Pitts (2012).

with Noel and Pitts (2012) bolsters confidence in our findings on corresponding chemical impacts, and is why we are using this threshold for comparison with the datasets in Sect. 3. Note that the simulation by Noel and Pitts (2012) started on 01 June 2008. The comparison with Noel and Pitts (2012) demonstrates that the new parametrization is able to represent specific mountain wave events and their intermittent character (e.g., Hertzog et al., 2012).

These temperature perturbations have impacts on several aspects of the chemistry in WACCM. The rows 6 to 8 of Fig. 8 show the timeseries of the surface area density (SAD) of ice, NAT and super-cooled ternary solutions (STS) for the four model cases. During periods with increased $\hat{T}$, there is also an increase of STS and NAT SADs. Especially at the start of the winter in May 2008 for the Antarctic Peninsula, the large-scale temperature is often too high to form PSCs, but with $\hat{T}$ applied they are formed. This is consistent with previous studies which found that mountain-wave-induced PSCs are most important at the start of the polar winter (e.g., McDonald et al., 2009).

The change in PSC surface area density as well as the direct temperature change and associated reactivity changes due to $\hat{T}$ then lead to changes in the chlorine and nitrogen compounds in the model, which are sometimes substantial (rows 1 to 5). Gaseous nitric acid (HNO_3, fifth row) is taken up by the aerosols and therefore decreases with the additional appearance of PSCs due to $\hat{T}$. N_2O_5 (fourth row) reacts on the surface of PSCs and is hence depleted during the events as a result of the $\hat{T}$ parametrization. The reactive chlorine species, summarized as ClO_x (first row) with

$$ClO_x = Cl + ClO + HOCl + 2\,Cl_2 + 2\,Cl_2O_2 + OClO \tag{7}$$

increase due to the increase in PSC SAD, whereas the reservoir species HCl (second row) is depleted as a consequence, which is known as chlorine activation (e.g., Solomon, 1999). HCl has a longer lifetime than the active chlorine species, which is why the changes are transported downstream of the mountain and persist longer than the gravity wave events themselves can be seen. The change in chlorine nitrate ($ClONO_2$, third row) depends on the availability of active chlorine and nitrogen. In both of these illustrative time series, $ClONO_2$ is increased as a result of $\hat{T}$, known as the "collar" formation (Solomon et al., 2016; Toon et al., 1989).

Although overall changes in the concentrations are relatively small, they can be locally as large as about 50 percent for some species and events. This underscores the importance of considering gravity wave processing in models that may seek to interpret airborne or other measurements. For example, attempts to infer the exact temperatures of chlorine activation processes based on field measurements may require consideration of gravity wave-driven perturbations. These are better simulated with the sub-stepping approach to ensure realistic simulation of nonlinear chemistry, since the large temperature fluctuations in successive time steps inherent in the stochastic approach can produce unrealistic transients in chemical composition on time scales comparable to the model's time step.

In summary, Figure 8 shows that the new parametrization is able to reflect specific gravity wave events with direct impact on the aerosols and the associated chemistry in the model. As expected from the scaling factor applied, the chemistry response is larger for the "Sub-stepping (non-scaled)" simulation compared with the REF case. The stochastic method is able to reproduce the chemistry impact of "Sub-stepping (scaled)" in all the time series shown, with minor differences in its amplitude on specific days.

Chemistry impacts are not only restricted to Svalbard and the Antarctic Peninsula, but occur at all known hot spots of orographic gravity waves in the model. Figure 9 shows global maps of the two-year maximum or minimum relative difference between "Sub-stepping (scaled)" and REF at 15 hPa for several species in the model. The largest relative differences are connected to the global hot spots of gravity waves, espe-

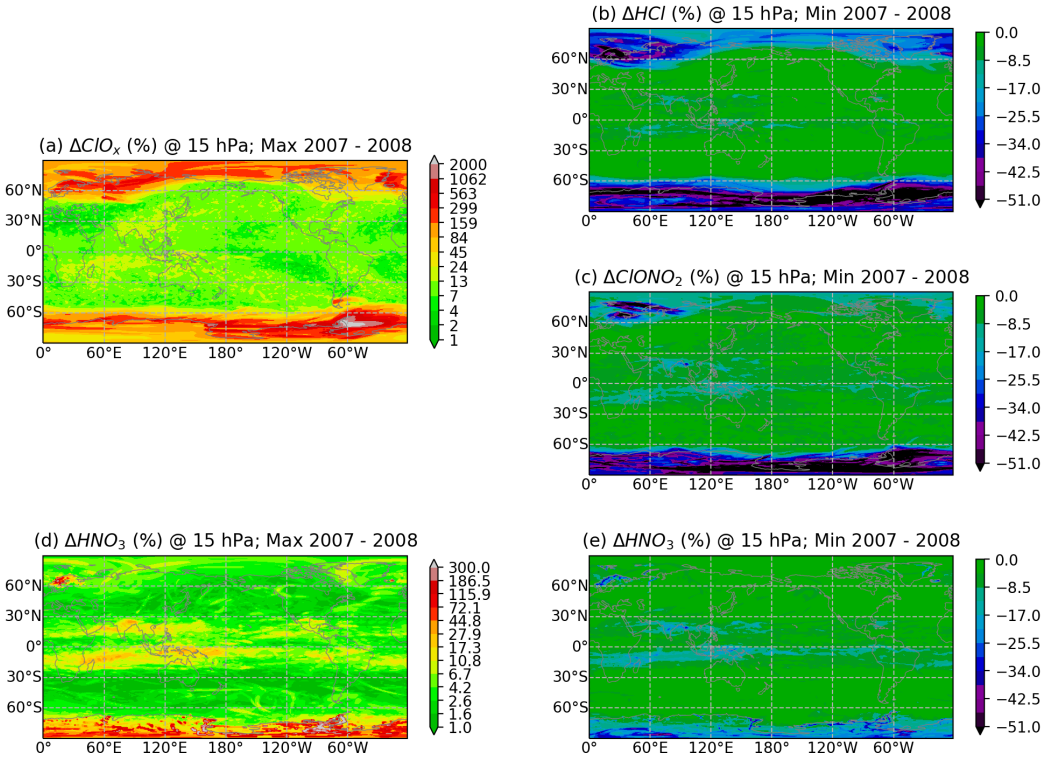

Figure 9. Two-year maximum (left column) and minimum (right column) relative difference between "Sub-stepping (scaled)" and "REF" simulations of daily averaged (a) ClO_x, (b) HCl, (c) $ClONO_2$ and (d,e) HNO_3 at 15 hPa.

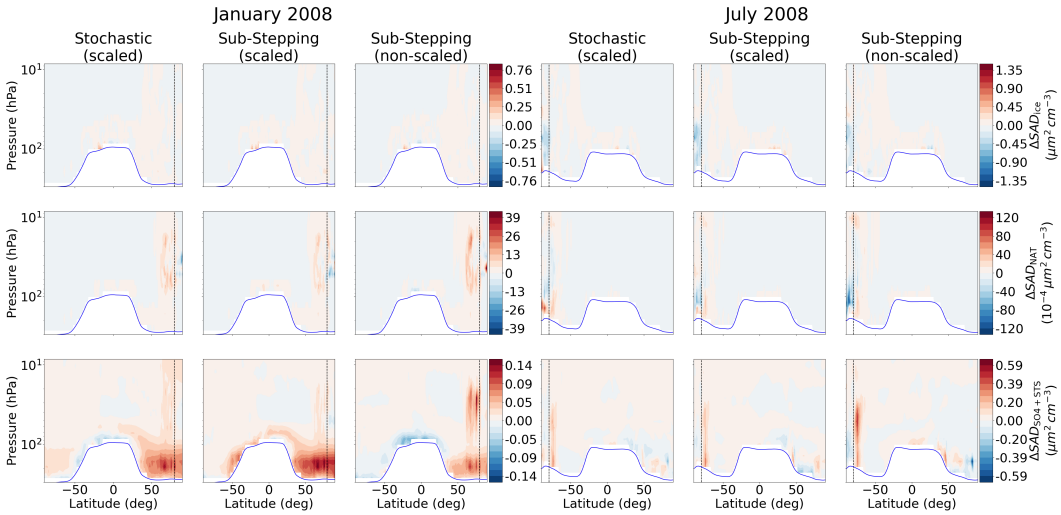

Figure 10. Zonal monthly mean difference between "Sub-stepping (scaled)" or "Sub-stepping (non-scaled)" and REF simulations in the stratosphere during January and July 2008 for ice (first row), NAT (second row) and STS (third row) SADs. The blue line shows the zonal mean tropopause height and the dashed black vertical line separates the polar night from the rest of the globe. Tropospheric values are whited out; see text for explanation. Please note the different color ranges for each month and variable.

cially for HNO_3 (panel d and e): Svalbard, Iceland, Scandinavian Mountains, Ural Mountains, Andes, Antarctic Peninsula and the edge of the Transantarctic Mountains. These mountain-wave-induced changes propagate downstream of the mountains, visible in the daily averaged results shown here. HCl (panel b) and $ClONO_2$ (panel c) have longer lifetimes than the active chlorine species so that the changes propagate further downstream, but there is still a connection to the noted hot spots of orographic gravity waves in their (negative) changes. As mentioned above, HNO_3 (panel d and e) is taken up by PSCs but it is also produced by heterogeneous reactions on the surface of PSCs (Solomon, 1999). That is why the largest positive and negative changes in HNO_3 can be found directly above the mountains, where $\hat{T}$ is largest, cf. Fig. 2, with maximum values locally larger than 350 % and minimum relative differences down to −54 %. Such substantial changes could confound interpretation of satellite or in-situ measurements of these species, if gravity wave-induced temperature perturbations are not fully taken into account.

Indeed, on some days in the simulations, chlorine is activated as a result of the $\hat{T}$ parametrization whereas no active chlorine was obtained without it. This is manifested by local maximum relative differences in ClO_x that can exceed 2000 %.

These large local changes are then transported downstream of the mountains and mixed with unperturbed air masses and lead to monthly mean changes. Figure 10 shows the zonal monthly mean differences in SAD of PSCs between the three $\hat{T}$ simulations and REF in January and July 2008. Both STS (third row) and NAT (second row) SADs show an increase in the polar region as a result of $\hat{T}$, which is expected from the non-linear growth of these particles at low temperatures (e.g., Carslaw et al., 1994). Ice (first row) concentrations are orders of magnitude larger in the troposphere than in the stratosphere. Since some grid points that contribute to the zonal mean at the tropopause are tropospheric and some points are stratospheric, the largest zonal mean differences relative to the control run occur at the tropopause. Zonal mean relative differences show larger increases at the edge of the polar vortex in both months, see Fig. S2 in the supplement.

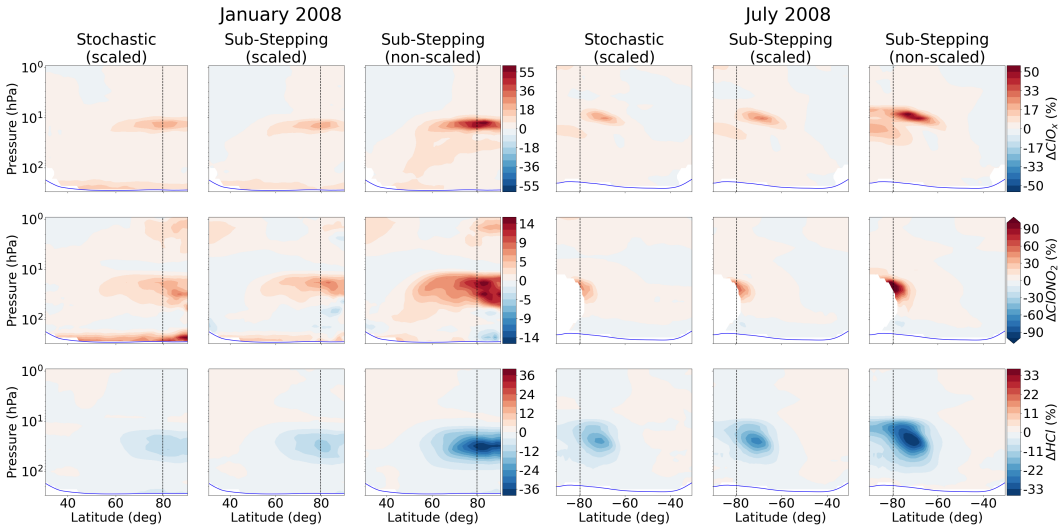

Figure 11. Zonal monthly mean relative differences for ClO_x (first row), $ClONO_2$ (second row) and HCl (third row) for the winter polar latitudes. Relative differences with absolute values lower than 1 pptv are removed from the analysis. Otherwise, same configuration as in Fig. 10.

Changes are also obtained in particle abundances (ice, NAT, and STS) near the tropical tropopause, where temperatures approach values as cold as the Antarctic vortex, particularly in the summer when monsoon heterogeneous chemistry can be significant (Solomon et al., 2016). This raises the potential for impacts on cirrus, and water vapor transport into the stratosphere, but these are beyond the scope of the present paper. The decrease of the STS SAD above the tropical tropopause in January 2008 can probably be explained by the lowest absolute temperatures combined with increased $\hat{T}$ values in this region where the warm phase of the OGW will significantly (and non-linearly) decrease the SAD of sulfates. In addition, the HNO_3 volume mixing ratio in the model is lower at the tropical tropopause region than in the polar winter, so that increases of the SAD due to lower temperature are not as large as in the polar regions (e.g., Carslaw et al., 1994, for the temperature and HNO_3 dependence of the SAD).

All species discussed in this section also show changes in the troposphere. These occur with irregular patterns as soon as something is changed in the applied parametrizations. To test the reason for this, a simulation randomly perturbing the initial temperature of REF on the order of 10^{-14} K, as done in previous work with CESM (Kay et al., 2015; Stone et al., 2019; Shah et al., 2022), led to similar tropospheric changes of these species, see Fig. S3 in the supplement for ozone. Thus, these changes are apparently a result of the dynamical changes due to slightly different solution of the chemistry equations in the model after adding the new parametrization, and the troposphere is therefore excluded from the analysis of this study. In the stratosphere, the mixing ratios of these species are larger and the time scales are longer than in the troposphere where they are partly determined by convective transport, so that these changes are relatively small in the stratosphere.

The changes in aerosol SAD as well as the change in temperature itself due to $\hat{T}$ result in changes of many gas-phase species. Figure 11 shows the zonal monthly mean relative changes of the chlorine species for the same months in the winter high latitudes. As expected from the timeseries in Fig. 8, both ClO_x and $ClONO_2$ are increased in the winter polar lower stratosphere whereas HCl is decreased. The changes are larger in the southern compared to the northern winter and depend on the scaling employed, which

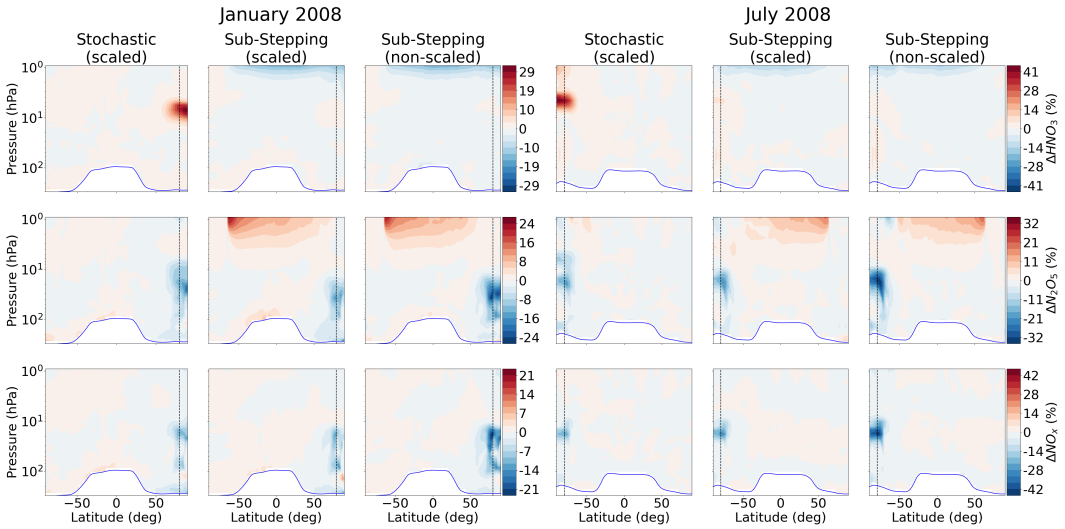

Figure 12. Zonal monthly mean relative differences for HNO_3 (first row), N_2O_5 (second row) and NO_x (third row). Otherwise, same configuration as Fig. 10.

emphasizes that the changes are due to $\hat{T}$ and not to other processes in the model. In the "Sub-stepping (scaled)" simulation, zonal monthly mean relative differences as high as 30 %, 50 % and −20 % can be found for ClO_x, $ClONO_2$ and HCl, respectively, in these regions. This implies substantial gravity wave-driven impacts that could influence interpretation of observations of those species. The monthly and zonally averaged stratospheric response in terms of chlorine activation is similar for the stochastic approach compared to "Sub-stepping (scaled)".

Many of the stratospheric changes are located at the edge of the polar vortex where gradients are large and temperatures approach the thresholds of PSC chemistry, and hence display an increased sensitivity to temperature changes. This is shown by the curved shape of the changes, especially for ClO_x and southern winter $ClONO_2$ and HCl. Since the northern hemisphere polar vortex is unstable compared to the southern hemisphere vortex, the changes in the longer-lived (and therefore transported) $ClONO_2$ and HCl are not as confined in latitude as those in the southern hemisphere.

The comparison of the "Sub-stepping (scaled)" and "Sub-stepping (non-scaled)" experiments demonstrates the importance of a correct representation of gravity wave temperature perturbations in the chemistry of WACCM. Although $\hat{T}$ is only increased by about 60 % the changes in ClO_x and HCl in the "Sub-stepping (non-scaled)" simulation are larger than the scaling factor in $\hat{T}$. This illustrates the non-linearity of the chemistry response on temperature changes.

Changes due to the gravity wave temperature perturbations can also be seen in the nitrogen-containing species, see Fig. 12 for the zonal monthly mean relative differences of HNO_3 (first row), N2O5 (second row) and NO_x (third row), where

$$NO_x = N + NO + NO_2 \tag{8}$$

As already discussed, the impact of temperature on the chemistry of HNO_3 is twofold, which is why the net effect in the lower stratosphere is small. In January 2008, the net relative differences near 30 hPa in the polar region are lower than 3 %. In July, the increase due to the heterogeneous reactions slightly dominates the uptake with relative differences around 6 % in the "Sub-stepping (non-scaled)" simulation. The increase of

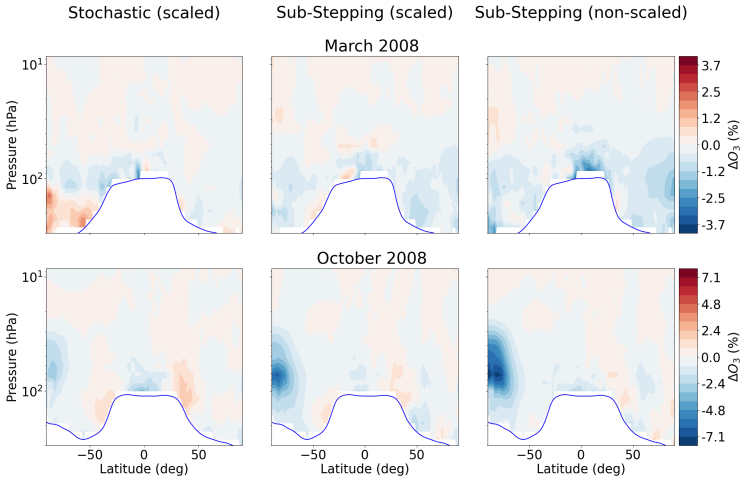

Figure 13. Same as Fig. 11 but for O_3 in March and October 2008.

HNO_3 in the "Stochastic (scaled)" simulation at around 7 hPa in the respective winter also occurs in the other simulations, but is one order of magnitude smaller. This can be explained by an increased SAD of aerosols in this region. N_2O_5 reacts with water vapor on the surface of PSCs, which is why the largest negative changes in the lower stratosphere are connected to the occurrence of PSCs and the chlorine chemistry, cf. Figs. 10 and 11. NO_x is a by-product of the N_2O_5 chemistry so that the changes on the order of around -20 to -45 % are correlated with that of N_2O_5.

Both HNO_3 and N_2O_5 in the "Sub-stepping (scaled)" and "Sub-stepping (non-scaled)" simulations show relative changes at around 1 hPa that do not change with the applied scaling factor. This effect can also be seen in species like OClO, HOCl, ClO (not shown). By sensitivity simulations that change the number of chemistry sub-steps but not the temperature it was found that these relative differences are a result of the sub-stepping rather than a physical effect. These artifacts are therefore removed when using the stochastic approach, where no sub-stepping is applied.

A number of these species can in principle influence ozone, but we find that effects on ozone are quite small at least in the monthly average. The impact on ozone in terms of zonal monthly mean relative differences is illustrated in Fig. 13. Generally, the impact on ozone is most prominent at the end of the polar ozone depletion season. Therefore, the relative changes for ozone are shown for March and October 2008. Since air masses subside in the polar vortex, the maximum lower stratospheric changes in ozone occur at lower altitudes than that of PSCs, chlorine and nitrogen species in the previous figures. At the end of the northern hemispheric winter, changes between -1 and -2 % can be related to the gravity wave temperature perturbation. In the southern hemisphere during October, the changes are larger with -3 to -8 % in the pressure range from about 100 to 30 hPa.

Monthly average negative changes in ozone occur all over the Antarctic Continent, as can be seen in terms of total column ozone in Fig. 14 averaged over all simulated October months. The changes are on the order of -2 to -4 DU in the "Sub-stepping (scaled)" and "Sub-stepping (non-scaled)" simulations and less than -1 DU in the "Stochastic (scaled)" simulation. Orr et al. (2020) found larger changes with their approach to account the interaction between OGWs and PSCs using the UK-UMCA model. They obtained local changes for October 2000 up to ± 7.5 DU. However, their simulation was free-running with boundary conditions for 2000 and these changes are a result of both chemistry and

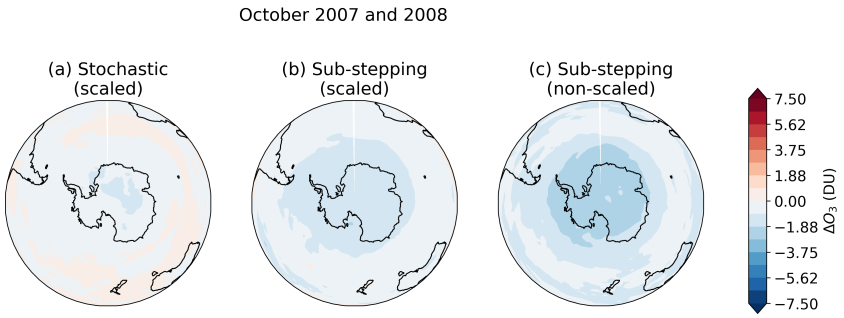

Figure 14. Average difference between (a) "Stochastic (scaled)", (b) "Sub-stepping (scaled)" or (c) "Sub-stepping (non-scaled)" and REF of total column ozone over the Antarctic Continent for October 2007 and 2008. Same colorbar as by Orr et al. (2020).

a horizontal shift of the polar vortex. Further, they applied the temperature change to PSCs only and the direct effect on the chemistry was missing. Perhaps most important, they accounted for the cold phase of the gravity wave only, while here we consider the full temporal evolution of the wave through its warm as well as cold phases, and the potential for cancellation between the two. The more nearly linear the chemistry is, the more complete the cancellation will be. On the other hand, nonlinear chemistry would be expected to yield a net effect. Hence, their simulations were a maximum estimate of the gravity wave effect.

In summary, we have shown in this section that the $\hat{T}$ parametrization leads to notable changes of the polar stratospheric chemistry at all known hot spots of orographic gravity waves on the globe. Gravity-wave-induced temperature changes lead to enhanced formation of aerosols and heterogeneous chemistry, resulting in increased chlorine activation and decreased polar ozone. Thus, this study enables the chemistry climate modeling community to account for this process in a consistent way.

5 Discussion and Conclusions

In this study, we developed a method to account for subgrid-scale gravity wave temperature perturbations in the chemistry on a global scale, a missing piece in chemistry-climate models. The method uses the subgrid-scale gravity momentum flux and large-scale parameters like the wind speed and the vertical gradient of the potential temperature to calculate a temperature perturbation amplitude due to gravity waves. This amplitude is then applied either by a sub-stepping of the chemistry with a sine-wave perturbation of the grid-scale temperature or by sine-wave distributed random temperature perturbations.

The temperature amplitudes $\hat{T}$ were compared with COSMIC satellite radio occultation measurements and ERA5 reanalysis data, which are both suitable datasets for information about gravity waves on a global scale. By comparing the $\hat{T}$ distributions of WACCM and the two datasets at altitudes between 14 and 34 km, we found that scaling factors between 1 and 0.6 depending upon altitude minimize the differences in the probability density distributions of the temperature perturbations. Since both COSMIC and ERA5 underestimate $\hat{T}$ for the shorter horizontal scale OGW, we tested effects of both scaled and unscaled WACCM sub-grid scale $\hat{T}$.

We presented various examples illustrating that the new parametrization leads to local as well as global changes in the model chemistry, many of which can be explained by the non-linear temperature dependence of both the formation of aerosols and asso-

ciated heterogeneous chemistry and the gas-phase chemistry. Some of these changes can be locally very large (much more than 100 %), which could influence interpretation of satellite or in-situ measurements. The parametrization is able to represent specific mountain wave events which enables future studies of the chemistry impact of local events even with a global model. The gravity wave temperature perturbations leads to increased chlorine activation and a corresponding reduction of species that react heterogeneously on PSCs as well as a zonal mean reduction of ozone between 3 and 8 % in the lower stratosphere.

The method as described in this study applies to orographic gravity waves only. An extension to non-orographic gravity waves would be desirable for the future, in order to be able to investigate the influence of weather systems like tropical storms, jets, fronts and convection on the chemistry (e.g., Wright, 2019; Zou et al., 2021).

For a comparison of the model with measurements, observations with appropriately high spatial resolution would be needed. Satellite measurements are typically averaged either in the vertical or in the horizontal and have to be averaged in time to reduce the signal-to-noise ratio which makes it difficult to see the chemistry changes shown in this study. Measurement campaigns like SOUTHTRAC-GW (Rapp et al., 2021) could help to assess and reduce errors in the model and compare the stochastic with the sub-stepping approach for specific case studies. While the sub-stepping of the chemistry decreases the overall performance of the model, it could be useful for detailed comparisons with airborne measurements where data at single time steps and grid points are needed. The stochastic approach leads to similar results on long-term averages but should not be used for comparisons at single grid points. Therefore, the latter could be useful for long-term simulations as it accounts for warm and cold phase of the gravity wave without impacting the model's computation time.

Consistent with previous studies like McDonald et al. (2009), the results of this study suggest that gravity-wave-induced temperature perturbations increase the period with chlorine activation, since we found the largest changes at the start and the end of the local winter. This work rises further questions that could be tackled by future simulations:

1. What is the impact of gravity wave temperature perturbations on ozone recovery?
2. What is the dynamical effect of this process in the model?
3. What are the impacts at altitudes higher than 1 hPa?

Our study focused on stratospheric chemistry, but there are also changes in the troposphere. Further work is needed to investigate the tropospheric changes as they appear to be associated with dynamical rather than chemical changes. The $\hat{T}$ values in the mesosphere are expected to be even larger. With a different model set-up, the changes at these altitudes in the model could also be investigated.

The response of WACCM's chemistry to the applied temperature perturbations is consistent with expectations from previous studies which were not able to account for this process on a global scale. The method should be easy to implement in other chemistry-climate models as well. We hope that this study assists other chemistry climate researchers who seek to account for subgrid-scale gravity wave temperature perturbations.

Appendix A Datasets

As discussed in Sect. 3, we compare the WACCM $\hat{T}$ with COSMIC satellite measurements and ERA5 reanalysis data which are briefly summarized in this section, to-

gether with the method to derive the gravity wave temperature perturbations from the temperature fields of each dataset.

A1 COSMIC

COSMIC (Rocken et al., 2000) provided high-precision global positioning system-based radio occultation measurements of temperature and humidity with an uncertainty of less than 1 K (Scherllin-Pirscher et al., 2011). Since the measuring satellite in low-Earth orbit could receive signals from whichever GPS satellite is in its view, the profiles are scattered irregularly in time and location on Earth. COSMIC provided nearly global coverage each day with higher density in the mid-latitudes (Wang & Alexander, 2010). Additionally, the vertical resolution of about 1 km for wave observations makes the measurements suitable for investigation of gravity waves in the atmosphere (e.g., Schmidt et al., 2016; Scherllin-Pirscher et al., 2021). The measurements are reliable in the stratosphere up to 38 km altitude (Wang & Alexander, 2010) and the mission covered the period from mid 2006 to mid 2020. Due to the limb-like viewing geometry of the satellite, horizontal resolution is limited to about 300 km (e.g., Kursinski et al., 1997). Depending on the orientation of the gravity wave to the line of sight, shorter scale gravity wave amplitudes are underestimated by radio occultation measurements, as described e.g. by Schmidt et al. (2016).

In order to derive gravity wave properties from the COSMIC temperature measurements, it is necessary to separate planetary waves, such as Kelvin and Rossby waves, from the gravity waves of interest here. We apply the method by Wang and Alexander (2010) to the COSMIC measurements which consists of a binning of the data to a 15x10 longitude-latitude grid for each level, applying a longitude-dependent Stockwell-transform (Stockwell et al., 1996) to each altitude and latitude bin, interpolating the temperatures back to the profile locations and subtracting this large-scale signal from the original measurements. The coverage of the measurements requires the large-scale temperature to be defined by zonal wavenumbers 0–6 (Wang & Alexander, 2010). Thus, this removes the largest wavelengths from the temperature, but remnants of planetary waves might still remain in the resulting temperature perturbations. As suggested by Wang and Alexander (2010), we bin the temperatures on a daily basis, but we use a sine fit or (where both are impossible) a nearest neighbor interpolation with four neighbors to fill remaining gaps. We use the "wet" temperature profiles which account for humidity and can therefore be used at lower altitudes than the dry profiles.

A2 ERA5

Since publication of the fifth generation reanalysis product by ECMWF ERA5 (Hersbach et al., 2020), it has been shown that it is able to directly resolve a large fraction of gravity waves (Dörnbrack, 2021; Dörnbrack et al., 2022; Kaifler et al., 2020) although it will be missing or underestimating amplitudes of short horizontal wavelength OGW (Hoffmann et al., 2017; Kruse et al., 2022). Therefore, it is suitable as a reference for gravity wave studies. In contrast to satellite measurements, it provides hourly global coverage.

In the method by Dörnbrack et al. (2022), gravity wave temperature perturbations are extracted from the ERA5 data by removing the truncation at 21 wavenumbers (T21) from the full spectral resolution output of ERA5. This ensures that the temperature perturbations consist of horizontal wavenumbers larger than 22, i.e. wavelengths smaller than about 1000 km at 60°S/N (Gupta et al., 2021). The horizontal grid spacing of 0.28125 degrees limits the possible analysis to wavelengths larger than about 160 km.

Gravity waves in ERA5 are damped starting at 1 hPa (Kaifler et al., 2020). In addition, the hybrid coordinates of ERA5 in the vertical induce large temperature pertur-

bations directly at mountain surface levels. In order to minimize both effects, we limit our analysis to pressure levels between 5 and 100 hPa.

Open Research

COSMIC data are downloaded from UCAR COSMIC Program (2006). ERA5 data are downloaded using the Climate Data Store (CDS) API (Hersbach et al., 2017). Model simulation data and the scripts used to create the figures are available online using the following link: `https://www.acom.ucar.edu/DOI-DATA/dkin/JAMES_Weimer_2022`. The model code (software) modifications to add the parametrization to the published version of CESM2.1.1 (see Danabasoglu et al., 2020) can also be found using this link.

Acknowledgments
This work is supported by grant no. AGS-1906719 from the Atmospheric Chemistry Division of the U.S. National Science Foundation (NSF). MJA is supported by NASA grant no. 80NSSC20K0950. This material is based upon work supported by National Center for Atmospheric Research (NCAR), which is a major facility sponsored by NSF under the Cooperative Agreement 1852977. Parts of this study are generated using Copernicus Climate Change Service information [2022]. Neither the European Commission nor ECMWF is responsible for any use that may be made of the Copernicus information or data it contains. The CESM project is supported primarily by NSF. We would like to acknowledge high-performance computing and data storage support from Cheyenne and Casper provided by NCAR's Computational and Information Systems Laboratory (2019), sponsored by NSF.

References

Alexander, M. J. (2015). Global and seasonal variations in three-dimensional gravity wave momentum flux from satellite limb-sounding temperatures. *Geophysical Research Letters*, *42*(16), 6860-6867. doi: https://doi.org/10.1002/2015GL065234

Alexander, S. P., Klekociuk, A. R., & Tsuda, T. (2009). Gravity wave and orographic wave activity observed around the Antarctic and Arctic stratospheric vortices by the COSMIC GPS-RO satellite constellation. *Journal of Geophysical Research: Atmospheres*, *114*(D17). doi: 10.1029/2009JD011851

Anthes, R. A., Bernhardt, P. A., Chen, Y., Cucurull, L., Dymond, K. F., Ector, D., ... Zeng, Z. (2008). The COSMIC/FORMOSAT-3 Mission: Early Results. *Bulletin of the American Meteorological Society*, *89*(3), 313 - 334. doi: 10.1175/BAMS-89-3-313

Bacmeister, J. T., Newman, P. A., Gary, B. L., & Chan, K. R. (1994). An Algorithm for Forecasting Mountain Wave-Related Turbulence in the Stratosphere. *Weather and Forecasting*, *9*(2), 241–253. doi: 10.1175/1520-0434(1994)009⟨0241:AAFFMW⟩2.0.CO;2

Burkholder, J. B., Sander, S. P., Abbatt, J. P. D., Barker, J. R., Huie, R. E., Kolb, C. E., ... Wine, P. H. (2015). *Chemical Kinetics and Photochemical Data for Use in Atmospheric Studies: Evaluation Number 18* (Tech. Rep.). Pasadena: Jet Propulsion Laboratory.

Carslaw, K. S., Luo, B. P., Clegg, S. L., Peter, T., Brimblecombe, P., & Crutzen, P. J. (1994). Stratospheric aerosol growth and HNO3 gas phase depletion from coupled HNO3 and water uptake by liquid particles. *Geophysical Research Letters*, *21*(23), 2479–2482. doi: 10.1029/94GL02799

Carslaw, K. S., Wirth, M., Tsias, A., Luo, B. P., Dörnbrack, A., Leutbecher, M., ... Peter, T. (1998). Increased stratospheric ozone depletion due to mountain-induced atmospheric waves. *Nature*, *391*(6668), 675–678. doi: 10.1038/35589

Computational and Information Systems Laboratory. (2019). *Cheyenne: HPE/SGI ICE XA System (University Community Computing)* (Tech. Rep.). Bolder, CO: National Center for Atmospheric Research. doi: 10.5065/D6RX99HX

Danabasoglu, G., Lamarque, J. F., Bacmeister, J., Bailey, D. A., DuVivier, A. K., Edwards, J., ... Strand, W. G. (2020). The Community Earth System Model Version 2 (CESM2). *Journal of Advances in Modeling Earth Systems*, *12*(2), e2019MS001916. doi: 10.1029/2019MS001916

Das, U., & Pan, C. J. (2013). Strong Kelvin wave activity observed during the westerly phase of QBO - A case study. *Annales Geophysicae*, *31*(4), 581–590. doi: 10.5194/ANGEO-31-581-2013

Dörnbrack, A. (2021). Stratospheric Mountain Waves Trailing across Northern Europe. *Journal of the Atmospheric Sciences*, *78*(9), 2835–2857. doi: 10.1175/JAS-D-20-0312.1

Dörnbrack, A., Eckermann, S. D., Williams, B. P., & Haggerty, J. (2022). Stratospheric Gravity Waves Excited by a Propagating Rossby Wave Train—A DEEPWAVE Case Study. *Journal of the Atmospheric Sciences*, *79*(2), 567–591. doi: 10.1175/JAS-D-21-0057.1

Dörnbrack, A., Gisinger, S., Pitts, M. C., Poole, L. R., & Maturilli, M. (2017). Multilevel Cloud Structures over Svalbard. *Monthly Weather Review*, *145*(4), 1149–1159. doi: 10.1175/MWR-D-16-0214.1

Dörnbrack, A., Kaifler, B., Kaifler, N., Rapp, M., Wildmann, N., Garhammer, M., ... Austin, E. J. (2020). Unusual appearance of mother-of-pearl clouds above El Calafate, Argentina (50°21'S, 72°16'W). *Weather*, *75*(12), 378–388. doi: 10.1002/wea.3863

Eckermann, S. D., Dörnbrack, A., Flentje, H., Vosper, S. B., Mahoney, M. J., Bui, T. P., & Carslaw, K. S. (2006). Mountain Wave-Induced Polar Stratospheric Cloud Forecasts for Aircraft Science Flights during SOLVE/THESEO 2000. *Weather and Forecasting*, *21*(1), 42–68. doi: 10.1175/WAF901.1

Emmons, L. K., Schwantes, R. H., Orlando, J. J., Tyndall, G., Kinnison, D., Lamarque, J.-F., ... Pétron, G. (2020). The Chemistry Mechanism in the Community Earth System Model Version 2 (CESM2). *Journal of Advances in Modeling Earth Systems*, *12*(4), e2019MS001882. doi: 10.1029/2019MS001882

Ern, M., Preusse, P., Alexander, M. J., & Warner, C. D. (2004). Absolute values of gravity wave momentum flux derived from satellite data. *Journal of Geophysical Research D: Atmospheres*, *109*(20). doi: 10.1029/2004JD004752

Eyring, V., Bony, S., Meehl, G. A., Senior, C. A., Stevens, B., Stouffer, R. J., & Taylor, K. E. (2016). Overview of the Coupled Model Intercomparison Project Phase 6 (CMIP6) experimental design and organization. *Geoscientific Model Development*, *9*(5), 1937–1958. doi: 10.5194/GMD-9-1937-2016

Fritts, D. C., & Alexander, J. M. (2003). Gravity wave dynamics and effects in the middle atmosphere. *Reviews of Geophysics*, *41*(1), 1003. doi: 10.1029/2001RG000106

Fueglistaler, S., Buss, S., Luo, B. P., Wernli, H., Flentje, H., Hostetler, C. A., ... Peter, T. (2003). Detailed modeling of mountain wave PSCs. *Atmospheric Chemistry and Physics*, *3*(3), 697–712. doi: 10.5194/acp-3-697-2003

Garcia, R. R., Smith, A. K., Kinnison, D. E., Cámara, A. d. l., & Murphy, D. J. (2017). Modification of the Gravity Wave Parameterization in the Whole Atmosphere Community Climate Model: Motivation and Results. *Journal of the Atmospheric Sciences*, *74*(1), 275–291. doi: 10.1175/JAS-D-16-0104.1

Gelaro, R., McCarty, W., Suárez, M. J., Todling, R., Molod, A., Takacs, L., ... Zhao, B. (2017). The Modern-Era Retrospective Analysis for Research and Applications, Version 2 (MERRA-2). *Journal of Climate*, *30*(14), 5419–5454. doi: 10.1175/JCLI-D-16-0758.1

Gettelman, A., Mills, M. J., Kinnison, D. E., Garcia, R. R., Smith, A. K., Marsh, D. R., ... Randel, W. J. (2019). The Whole Atmosphere Community Climate

Model Version 6 (WACCM6). *Journal of Geophysical Research: Atmospheres*, *124*(23), 12380–12403. doi: 10.1029/2019JD030943

Giorgetta, M. A., Brokopf, R., Crueger, T., Esch, M., Fiedler, S., Helmert, J., ... Stevens, B. (2018). ICON-A, the Atmosphere Component of the ICON Earth System Model: I. Model Description. *Journal of Advances in Modeling Earth Systems*, *10*(7), 1613-1637. doi: https://doi.org/10.1029/2017MS001242

Gupta, A., Birner, T., Dörnbrack, A., & Polichtchouk, I. (2021). Importance of Gravity Wave Forcing for Springtime Southern Polar Vortex Breakdown as Revealed by ERA5. *Geophysical Research Letters*, *48*(10), e2021GL092762. doi: 10.1029/2021GL092762

Hanson, D., & Mauersberger, K. (1988). Laboratory studies of the nitric acid trihydrate: Implications for the south polar stratosphere. *Geophysical Research Letters*, *15*(8), 855–858. doi: 10.1029/GL015I008P00855

Hersbach, H., Bell, B., Berrisford, P., Hirahara, S., Horányi, A., Muñoz Sabater, J., ... Thépaut, J.-N. (2020). The ERA5 global reanalysis. *Quarterly Journal of the Royal Meteorological Society*, *146*(730), 1999-2049. doi: https://doi.org/10.1002/qj.3803

Hersbach, H., Bell, B., Berrisford, P., Hirahara, S., Horányi, A., Muñoz-Sabater, J., ... Thépaut, J.-N. (2017). Complete ERA5: Fifth generation of ECMWF atmospheric reanalyses of the global climate. *Copernicus Climate Change Service (C3S) Data Store (CDS)*. (Accessed on 01-Feb-2022)

Hertzog, A., Alexander, J. M., & Plougonven, R. (2012). On the Intermittency of Gravity Wave Momentum Flux in the Stratosphere. *Journal of the Atmospheric Sciences*, *69*(11), 3433–3448. doi: 10.1175/JAS-D-12-09.1

Hoffmann, L., & Alexander, M. J. (2009). Retrieval of stratospheric temperatures from Atmospheric Infrared Sounder radiance measurements for gravity wave studies. *Journal of Geophysical Research*, *114*(D7), D07105. doi: 10.1029/2008JD011241

Hoffmann, L., Günther, G., Li, D., Stein, O., Wu, X., Griessbach, S., ... Wright, J. S. (2019). From ERA-Interim to ERA5: the considerable impact of ECMWF's next-generation reanalysis on Lagrangian transport simulations. *Atmospheric Chemistry and Physics*, *19*(5), 3097–3124. doi: 10.5194/acp-19-3097-2019

Hoffmann, L., Spang, R., Orr, A., Alexander, M. J., Holt, L. A., & Stein, O. (2017). A decadal satellite record of gravity wave activity in the lower stratosphere to study polar stratospheric cloud formation. *Atmospheric Chemistry and Physics*, *17*(4), 2901–2920. doi: 10.5194/acp-17-2901-2017

Hoffmann, L., Xue, X., & Alexander, M. J. (2013). A global view of stratospheric gravity wave hotspots located with Atmospheric Infrared Sounder observations. *Journal of Geophysical Research: Atmospheres*, *118*(2), 416–434. doi: 10.1029/2012JD018658

Jackson, D. R., Gadian, A., Hindley, N. P., Hoffmann, L., Hughes, J., King, J., ... Mitchell, N. J. (2018). The South Georgia Wave Experiment: A Means for Improved Analysis of Gravity Waves and Low-Level Wind Impacts Generated from Mountainous Islands. *Bulletin of the American Meteorological Society*, *99*(5), 1027–1040. doi: 10.1175/BAMS-D-16-0151.1

Kaifler, N., Kaifler, B., Dörnbrack, A., Rapp, M., Hormaechea, J. L., & de la Torre, A. (2020). Lidar observations of large-amplitude mountain waves in the stratosphere above Tierra del Fuego, Argentina. *Scientific Reports 2020 10:1*, *10*(1), 1–10. doi: 10.1038/s41598-020-71443-7

Kärcher, B., Jensen, E. J., & Lohmann, U. (2019). The impact of mesoscale gravity waves on homogeneous ice nucleation in cirrus clouds. *Geophysical Research Letters*, *46*(10), 5556-5565. doi: https://doi.org/10.1029/2019GL082437

Kay, J. E., Deser, C., Phillips, A., Mai, A., Hannay, C., Strand, G., ... Vertenstein, M. (2015). The Community Earth System Model (CESM) Large Ensemble

Project: A Community Resource for Studying Climate Change in the Presence of Internal Climate Variability. *Bulletin of the American Meteorological Society*, *96*(8), 1333 - 1349. doi: 10.1175/BAMS-D-13-00255.1

Kinnison, D. E., Brasseur, G. P., Walters, S., Garcia, R. R., Marsh, D. R., Sassi, F., ... Simmons, A. J. (2007). Sensitivity of chemical tracers to meteorological parameters in the MOZART-3 chemical transport model. *Journal of Geophysical Research: Atmospheres*, *112*(D20), 20302. doi: 10.1029/2006JD007879

Knippertz, P., Gehne, M., Kiladis, G. N., Kikuchi, K., Satheesh, A. R., Roundy, P. E., ... Wheeler, M. C. (2022). The intricacies of identifying equatorial waves. *Quarterly Journal of the Royal Meteorological Society*. doi: 10.1002/QJ.4338

Krisch, I., Preusse, P., Ungermann, J., Dörnbrack, A., Eckermann, S. D., Ern, M., ... Riese, M. (2017). First tomographic observations of gravity waves by the infrared limb imager GLORIA. *Atmospheric Chemistry and Physics*, *17*(24), 14937–14953. doi: 10.5194/ACP-17-14937-2017

Kruse, C. G., Alexander, M. J., Hoffmann, L., van Niekerk, A., Polichtchouk, I., Bacmeister, J. T., ... Stein, O. (2022). Observed and Modeled Mountain Waves from the Surface to the Mesosphere near the Drake Passage. *Journal of the Atmospheric Sciences*, *79*(4), 909 - 932. doi: 10.1175/JAS-D-21-0252.1

Kursinski, E. R., Hajj, G. A., Schofield, J. T., Linfield, R. P., & Hardy, K. R. (1997). Observing Earth's atmosphere with radio occultation measurements using the Global Positioning System. *Journal of Geophysical Research: Atmospheres*, *102*(D19), 23429–23465. doi: 10.1029/97JD01569

Leena, P. P., Venkat Ratnam, M., Krishna Murthy, B. V., & Vijaya Bhaskara Rao, S. (2012). Detection of high frequency gravity waves using high resolution radiosonde observations. *Journal of Atmospheric and Solar-Terrestrial Physics*, *77*, 254–259. doi: 10.1016/J.JASTP.2012.01.003

Lilly, D. K., Nicholls, J. M., Kennedy, P. J., Klemp, J. B., & Chervin, R. M. (1982). Aircraft measurements of wave momentum flux over the Colorado Rocky Mountains. *Quarterly Journal of the Royal Meteorological Society*, *108*(457), 625–642. doi: 10.1002/QJ.49710845709

Madden, R. A. (1979). Observations of large-scale traveling Rossby waves. *Reviews of Geophysics*, *17*(8), 1935–1949. doi: 10.1029/RG017I008P01935

Mann, G. W., Carslaw, K. S., Chipperfield, M. P., Davies, S., & Eckermann, S. D. (2005). Large nitric acid trihydrate particles and denitrification caused by mountain waves in the Arctic stratosphere. *Journal of Geophysical Research*, *110*(D8), D08202. doi: 10.1029/2004JD005271

Marti, J., & Mauersberger, K. (1993). A survey and new measurements of ice vapor pressure at temperatures between 170 and 250K. *Geophysical Research Letters*, *20*(5), 363–366. doi: 10.1029/93GL00105

McDonald, A. J., George, S. E., & Woollands, R. M. (2009). Can gravity waves significantly impact PSC occurrence in the Antarctic? *Atmospheric Chemistry and Physics*, *9*(22), 8825–8840. doi: 10.5194/acp-9-8825-2009

McFarlane, N. A. (1987). The Effect of Orographically Excited Gravity Wave Drag on the General Circulation of the Lower Stratosphere and Troposphere. *Journal of Atmospheric Sciences*, *44*(14), 1775 - 1800. doi: 10.1175/1520-0469(1987)044⟨1775:TEOOEG⟩2.0.CO;2

Murphy, D. M., & Ravishankara, A. R. (1994). Temperature averages and rates of stratospheric reactions. *Geophysical Research Letters*, *21*(23), 2471–2474. doi: 10.1029/94GL02287

Noel, V., & Pitts, M. (2012). Gravity wave events from mesoscale simulations, compared to polar stratospheric clouds observed from spaceborne lidar over the Antarctic Peninsula. *Journal of Geophysical Research: Atmos.*, *117*(D11). doi: 10.1029/2011JD017318

Orr, A., Hosking, J. S., Delon, A., Hoffmann, L., Spang, R., Moffat-Griffin, T., ...

Braesicke, P. (2020). Polar stratospheric clouds initiated by mountain waves in a global chemistry–climate model: a missing piece in fully modelling polar stratospheric ozone depletion. *Atmospheric Chemistry and Physics*, *20*(21), 12483–12497. doi: 10.5194/acp-20-12483-2020

Polichtchouk, I., van Niekerk, A., & Wedi, N. (2022). Resolved gravity waves in the extra-tropical stratosphere: Effect of horizontal resolution increase from O(10 km) to O(1 km). *Journal of the Atmospheric Sciences*. doi: 10.1175/JAS-D-22-0138.1

Rapp, M., Kaifler, B., Dörnbrack, A., Gisinger, S., Mixa, T., Reichert, R., ... Engel, A. (2021). SOUTHTRAC-GW: An Airborne Field Campaign to Explore Gravity Wave Dynamics at the World's Strongest Hotspot. *Bulletin of the American Meteorological Society*, *102*(4), E871-E893. doi: 10.1175/BAMS-D-20-0034.1

Richter, J. H., Sassi, F., & Garcia, R. R. (2010). Toward a physically based gravity wave source parameterization in a general circulation model. *Journal of the Atmospheric Sciences*, *67*(1), 136 - 156. doi: 10.1175/2009JAS3112.1

Rocken, C., Kuo, Y. H., Schreiner, W. S., Hunt, D., Sokolovskiy, S., & McCormick, C. (2000). COSMIC system description. *Terrestrial, Atmospheric and Oceanic Sciences*, *11*(1), 21–52. doi: 10.3319/TAO.2000.11.1.21(COSMIC)

Scherllin-Pirscher, B., Steiner, A. K., Anthes, R. A., Alexander, M. J., Alexander, S. P., Biondi, R., ... Zeng, Z. (2021). *Tropical temperature variability in the UTLS: New insights from GPS radio occultation observations* (Vol. 34) (No. 8). American Meteorological Society. doi: 10.1175/JCLI-D-20-0385.1

Scherllin-Pirscher, B., Steiner, A. K., Kirchengast, G., Kuo, Y.-H., & Foelsche, U. (2011). Empirical analysis and modeling of errors of atmospheric profiles from gps radio occultation. *Atmospheric Measurement Techniques*, *4*(9), 1875–1890. doi: 10.5194/amt-4-1875-2011

Schmidt, T., Alexander, P., & de la Torre, A. (2016). Stratospheric gravity wave momentum flux from radio occultations. *Journal of Geophysical Research: Atmospheres*, *121*(9), 4443–4467. doi: 10.1002/2015JD024135

Shah, K., Solomon, S., Kinnison, D., Fu, Q., & Thompson, D. W. (2022). Phase unlocking and the modulation of tropopause-level trace gas advection by the quasibiennial oscillation. *Journal of Geophysical Research: Atmospheres*, *127*, e2021JD036142. (e2021JD036142) doi: https://doi.org/10.1029/2021JD036142

Smith, R. B., & Kruse, C. G. (2017). Broad-spectrum mountain waves. *Journal of the Atmospheric Sciences*, *74*(5), 1381 - 1402. doi: 10.1175/JAS-D-16-0297.1

Smith, R. B., & Kruse, C. G. (2018). A gravity wave drag matrix for complex terrain. *Journal of the Atmospheric Sciences*, *75*(8), 2599 - 2613. doi: 10.1175/JAS-D-17-0380.1

Solomon, S. (1999). Stratospheric ozone depletion: A review of concepts and history. *Reviews of Geophysics*, *37*(3), 275–316. doi: 10.1029/1999RG900008

Solomon, S., Kinnison, D., Bandoro, J., & Garcia, R. (2015). Simulation of polar ozone depletion: An update. *Journal of Geophysical Research: Atmos.*, *120*(15), 7958–7974. doi: 10.1002/2015JD023365

Solomon, S., Kinnison, D., Garcia, R. R., Bandoro, J., Mills, M., Wilka, C., ... Höpfner, M. (2016). Monsoon circulations and tropical heterogeneous chlorine chemistry in the stratosphere. *Geophysical Research Letters*, *43*(24), 12,624–12,633. doi: 10.1002/2016GL071778

Stockwell, R., Mansinha, L., & Lowe, R. (1996). Localization of the complex spectrum: the S transform. *IEEE Transactions on Signal Processing*, *44*(4), 998–1001. doi: 10.1109/78.492555

Stone, K. A., Solomon, S., Kinnison, D. E., Baggett, C. F., & Barnes, E. A. (2019). Prediction of northern hemisphere regional surface temperatures using stratospheric ozone information. *Journal of Geophysical Research: Atmospheres*,

124(12), 5922-5933. doi: https://doi.org/10.1029/2018JD029626

Taylor, M. J., Pautet, P. D., Fritts, D. C., Kaifler, B., Smith, S. M., Zhao, Y., ... Russell, J. M. (2019). Large-Amplitude Mountain Waves in the Mesosphere Observed on 21 June 2014 During DEEPWAVE: 1. Wave Development, Scales, Momentum Fluxes, and Environmental Sensitivity. *Journal of Geophysical Research: Atmospheres*, *124*(19), 10364–10384. doi: 10.1029/2019JD030932

Toon, G. C., Farmer, C. B., Lowes, L. L., Schaper, P. W., Blavier, J.-F., & Norton, R. H. (1989). Infrared aircraft measurements of stratospheric composition over Antarctica during September 1987. *Journal of Geophysical Research: Atmospheres*, *94*(D14), 16571-16596. doi: https://doi.org/10.1029/JD094iD14p16571

UCAR COSMIC Program. (2006). *COSMIC-1 Data Products [Data Set]* (Tech. Rep.). UCAR/NCAR - COSMIC. Retrieved from `https://doi.org/10.5065/ZD80-KD74`

Vosper, S. B., van Niekerk, A., Elvidge, A., Sandu, I., & Beljaars, A. (2020). What can we learn about orographic drag parametrisation from high-resolution models? A case study over the Rocky Mountains. *Quarterly Journal of the Royal Meteorological Society*, *146*(727), 979–995. doi: 10.1002/QJ.3720

Wang, L., & Alexander, M. J. (2010). Global estimates of gravity wave parameters from GPS radio occultation temperature data. *Journal of Geophysical Research: Atmospheres*, *115*(D21). doi: https://doi.org/10.1029/2010JD013860

Wegner, T., Kinnison, D. E., Garcia, R. R., & Solomon, S. (2013). Simulation of polar stratospheric clouds in the specified dynamics version of the whole atmosphere community climate model. *Journal of Geophysical Research: Atmospheres*, *118*(10), 4991–5002. doi: 10.1002/jgrd.50415

Weimer, M., Buchmüller, J., Hoffmann, L., Kirner, O., Luo, B., Ruhnke, R., ... Braesicke, P. (2021). Mountain-wave-induced polar stratospheric clouds and their representation in the global chemistry model ICON-ART. *Atmospheric Chemistry and Physics*, *21*(12), 9515–9543. doi: 10.5194/ACP-21-9515-2021

Wright, C. J. (2019). Quantifying the global impact of tropical cyclone-associated gravity waves using HIRDLS, MLS, SABER and IBTrACS data. *Quarterly Journal of the Royal Meteorological Society*, *145*(724), 3023–3039. doi: 10.1002/QJ.3602

Zou, L., Hoffmann, L., Griessbach, S., Spang, R., & Wang, L. (2021). Empirical evidence for deep convection being a major source of stratospheric ice clouds over North America. *Atmospheric Chemistry and Physics*, *21*(13), 10457–10475. doi: 10.5194/ACP-21-10457-2021